Eliminating Unwanted Far-Field Excitation in Objective-Type TIRF. Part I. Identifying Sources of Nonevanescent Excitation Light

Maia Brunstein,[†‡§] Maxime Teremetz,[†‡§¶] Karine Hérault,[†‡§] Christophe Tourain,[†‡§||] and Martin Oheim[†‡§*]
[†]CNRS, UMR 8154, Paris, F-75006 France; [‡]INSERM, U603, Paris, F-75006 France; [§]Laboratoire de Neurophysiologie et Nouvelles Microscopies, Université Paris Descartes, PRES Sorbonne Paris Cité, Paris, F-75006 France; [¶]Master Programme: Biologie Cellulaire, Physiologie et Pathologies (BCPP), Université Paris Diderot, PRES Sorbonne Paris Cité, Paris, France; and [||]Service Commun de Microscopie (SCM), Institut Fédératif de Recherche en Neurosciences, Paris, F-75006 France

ABSTRACT Total internal reflection fluorescence microscopy (TIRFM) achieves subdiffraction axial sectioning by confining fluorophore excitation to a thin layer close to the cell/substrate boundary. However, it is often unknown how thin this light sheet actually is. Particularly in objective-type TIRFM, large deviations from the exponential intensity decay expected for pure evanescence have been reported. Nonevanescent excitation light diminishes the optical sectioning effect, reduces contrast, and renders TIRFM-image quantification uncertain. To identify the sources of this unwanted fluorescence excitation in deeper sample layers, we here combine azimuthal and polar beam scanning (spinning TIRF), atomic force microscopy, and wavefront analysis of beams passing through the objective periphery. Using a variety of intracellular fluorescent labels as well as negative staining experiments to measure cell-induced scattering, we find that azimuthal beam spinning produces TIRFM images that more accurately portray the real fluorophore distribution, but these images are still hampered by far-field excitation. Furthermore, although clearly measureable, cell-induced scattering is not the dominant source of far-field excitation light in objective-type TIRF, at least for most types of weakly scattering cells. It is the microscope illumination optical path that produces a large cell- and beam-angle invariant stray excitation that is insensitive to beam scanning. This instrument-induced glare is produced far from the sample plane, inside the microscope illumination optical path. We identify stray reflections and high-numerical aperture aberrations of the TIRF objective as one important source. This work is accompanied by a companion paper (Pt.2/2).

INTRODUCTION

Among the techniques used to study membrane dynamics and organization, total internal reflection fluorescence microscopy (TIRFM) occupies a central place. TIRFM is a wide-field technique that confines fluorescence excitation to a thin, near-substrate layer defined by the axial intensity decay of the evanescent wave (EW) generated by total internal reflection. Confinement of fluorescence excitation reduces background and photobleaching and it is the basis for single-molecule detection, near-membrane fluorescence correlation spectroscopy, as well as membrane-selective photoactivation/photobleaching assays and a growing number of super-resolution microscopies (1–5) that rely on an axially well-defined excitation volume.

For TIRF light must hit a dielectric interface at a supercritical angle $\theta > \text{asin}\,(n_1/n_2)$. Here, n_1 and n_2 are, respectively, the refractive indices of the sample and substrate at the excitation wavelength λ. For a simple glass/water interface the EW penetration depth is calculated as $\delta(\theta) = \lambda/[4\pi(n_2^2\sin^2\theta - n_1^2)^{1/2}]$. Its actual value is often unknown because cells grown on a coverslip introduce a laminar structure consisting of at least four layers: glass:medium:membrane:cytoplasm. This sandwich modifies the axial decay of the EW intensity and its θ-dependence, but, at least in principle, in a predictable manner (6). However, δ also varies laterally, across the field of view, because cell adhesion and refractive index vary locally. Collectively, these effects make the quantitative interpretation of TIRF intensities uncertain (7–9). In practice, things are even worse because a significant fraction of the illumination reaches out to a larger depth than would be expected by pure evanescence. Nonevanescent excitation light is seen in the far field when looking from above at the microscope. How much of this far-field light propagates across the field-of-view and excites detectable fluorescence in deeper sample layers is unclear. For the now commonly used prismless (objective-type) configuration of TIRF (10,11), Mattheyses and Axelrod estimated a relative contribution of far-field excitation to ~10–15% at the reflecting interface and proportionally more at greater depths where the EW intensity has decayed (12).

The development of techniques that produce a more homogenous and localized EW excitation has been the topic of much research. In most laser-based TIRF microscopes, a single laser beam is focused to a tight spot in an eccentric position in the back focal plane (BFP) of a high-numerical aperture (NA) objective. This arrangement produces an EW that propagates across the field-of-view and introduces directionality in the image. Changing the polar beam angle θ varies the EW penetration depth (i.e., the volume probed by

Submitted November 15, 2013, and accepted for publication December 23, 2013.

*Correspondence: martin.oheim@parisdescartes.fr

Maia Brunstein's present address is the Laboratoire de Photonique et de Nanostructures (LPN-CNRS), Route de Nozay, F-91460 Marcoussis, France.

Martin Oheim's present address is the Brain Physiology Laboratory (CNRS UMR8118), 45 rue des Saints Pères, Paris, F-75006 France.

Editor: David Piston.

0006-3495/14/03/1020/13 $2.00

http://dx.doi.org/10.1016/j.bpj.2013.12.049

the EW) while changing the azimuth ϕ changes the orientation of EW propagation. Therefore, ring illumination (10) restores symmetry, but it is unsuitable for coherent laser light because interference generates a split focus useful for confocal spot detection but not for wide-field TIRFM imaging. Alternatively, isotropic EW illumination can also be produced by spinning the focused spot at a constant radius in the BFP, provided that the scan is fast compared to the of image acquisition (13–15). Time averaging over different EW propagation directions produces a more even illumination and facilitates image quantification (16). Although currently not much biological data are available with spinning TIRF (spTIRF) excitation, beam-scanning devices have been integrated in at least two commercial TIRF microscopes, the iLas2 from Roper Scientific and TILL/FEI's iMIC with the Polytrope illuminator.

This study was designed to answer three simple questions: 1), does beam spinning improve optical sectioning in biological TIRFM? 2), Even though beam scanning diminishes directional effects resulting from forward scattering, is this cell-induced scattering the dominant source of propagating excitation light? 3), Given the common observation that prism-type TIRF produces crisper images than objective-type TIRF, what is the role of the microscope excitation optical path and of the high-NA TIRF objective, in particular, in generating spurious stray excitation?

To answer these questions, we combined acoustooptic beam spinning (14), negative-staining imaging of unlabeled cells embedded in a fluorescein-dextran containing extracellular medium, atomic force microscopy (AFM), and optical wave-front analysis of high-NA beams to identify sample coverslip and instrument parameters that contribute to the loss of excitation confinement in objective-type TIRFM. We show that although beam spinning produces more evenly lit TIRFM images, it fails to better confine excitation axially. The reason is that (at least for a majority of cells that are weak scatterers) most contaminating excitation is generated far from the sample and comes from the beam delivery optics and the microscope objective itself (stray light and high-NA aberrations), rather than from EW scattering at irregularities of the reflecting interface or at organelles having a higher refractive index than the surrounding cytoplasm.

MATERIALS AND METHODS

Coverslips, dyes, and beads

No. 1 and No. 1.5 BK-7 coverslips (25-mm diameter, Schott-Desag D263M, Thermo Fisher Menzel, Braunschweig, Germany; measured thickness 147.8 ± 2.8 μm and 173.6 ± 2.8 μm, respectively, $n = 35$ each) as well as fused silica substrates (TGP, Painesville, OH) were sequentially passed twice through baths of 70% EtOH and sterile water, respectively, and were used thereafter. Otherwise, they were coated with polyornithine (1.5 μg/ml, 30 min, 37°C, 5% CO_2) or collagen (Glass and rat tail acid soluble Bornstein Traub type I collagen, Sigma, Lyon, France). Collagen was prepared at 1 mg/ml in aq. 1% acetic acid. This stock was diluted 1:200 in 30% EtOH and the coverslips incubated 3 h at room temperature (RT, 22–23°C), the excess liquid removed, and the coverslips dried (30 min, RT) under a dust-free air flow before use. Coverslips were stored individually in sealed 6-well plates (Dutscher, Brumath, France).

Submicron layers of rhodamine 6G (R6G, Sigma) or fluorescein isothiocyanate (FITC, Fluka, Buchs, Switzerland) were deposited on coverslips with a spin coater (KW-4A, SPI Supplies, West Chester, PA) at 3,000 rpm. Dilute solutions of red-emitting polystyrene latex microspheres (488/685 nm TransFluoSpheres, 93-nm diameter (∅), Invitrogen, Saint Aubin, France) were drop-cast onto a clean coverslip, immobilized by solvent evaporation, and used for point spread function measurements. Pixel size for point spread function measurements was 77 nm. Refractive indices n_D^{22-23} of immersion liquids were measured at 589 nm and RT) with an Abbe refractometer (WYA, Shanghai, China; Table S1 in the Supporting Material).

Cell preparation

Experiments followed EU and institutional guidelines for the care and use of laboratory animals (Council directive 86/609EEC). Astrocytes were prepared as described before (17) from P0-1 (P0 being the day of birth) NMRI mice (Janvier, Montpellier, France). Briefly, neocortices were dissected and mechanically dissociated. Cells were plated and maintained in petri dishes for 1 week to reach confluence before their transfer onto polyornithine-coated BK-7 coverslips. Secondary cultures were maintained in Dulbecco's modified Eagle medium (DMEM), supplemented with 5% fetal bovine serum (FBS), penicillin (5 units/ml), and streptomycin (5 μg/ml) at 37°C in a humidified 5% CO_2 atmosphere. Astrocytes were kept for 1 more week in secondary culture before imaging, during which they were continuously perfused at 1.5 ml/min with extracellular saline containing, in mM: 140 NaCl, 5.5 KCl, 1.8 $CaCl_2$, 1 $MgCl_2$, 20 glucose, 10 HEPES (pH 7.3, adjusted with NaOH). In secondary culture, astrocytes adopt a fibroblast-like polygonal shape. We used these flat and fairly transparent cells as an example of a weakly scattering cell. Astrocytes were incubated with FM2-10/FM4-64 to label lysosomes (17) and imaged after a 20 min wash. Alternatively, transfection with plasmids encoding VAMP2-EGFP, mito-EGFP, Lck-EGFP, vinculin-GFP, or CD63-GFP (see Table S2) produced small-vesicle-, mitochondrial-, plasma membrane-, cell adhesion site- or, again, lysosomal-staining, respectively. Transfected astrocytes were imaged 24–36 h following transfection.

BON cells were a gift from Dr C. Desnos (CNRS UMR8192, University Paris Descartes). The BON cell line was established from a lymph node metastasis of a human pancreatic carcinoid tumor provided to CNRS by Dr C. M. Townsend at the University of Texas, Medical Branch, Galveston, TX. BON cells were cultured in Ham's F-12/DMEM with 10% FBS and seeded onto collagen-coated glass coverslips. Isolated round cells were imaged 1–5 days after plating. We used BON cells that, similar to other neuroendocrine cells contain thousands of large dense-core secretory granules, as an example of a strongly scattering cell.

spTIRF microscopy

We adjusted the polar and azimuthal angle (θ,ϕ) of a 488-nm beam (Ar^+-ion laser Reliant 150; LaserPhysics, West Jordan, UT) impinging at the cell/substrate interface with a pair of acoustooptical deflectors (AODs, AA.Opto, St-Rémy-en-Chevreuse, France). A high-quality six-element scan lens (Rodagon, Rodenstock, Feldkirchen, Germany) focused the beam to a tight spot in the objective BFP, Fig. 1. All objectives used had NAs >1.45 and were piezo positioned to allow accurate focusing (PIFOC, Physik Instrumente, Karlsruhe, Germany). Fluorescence was detected through the same objective as that used for TIRF excitation and extracted with a dichroic (zt491 RDCXT, AHF, Tübingen, Germany) and band-pass filters listed in Table S3 on electron multiplying charge-coupled device cameras (EMCCD, Cascade 128+ or QuantEM512C, both from Photometrics, Tucson, AZ). Total magnifications were 80, 103, or 120 nm/pixel as

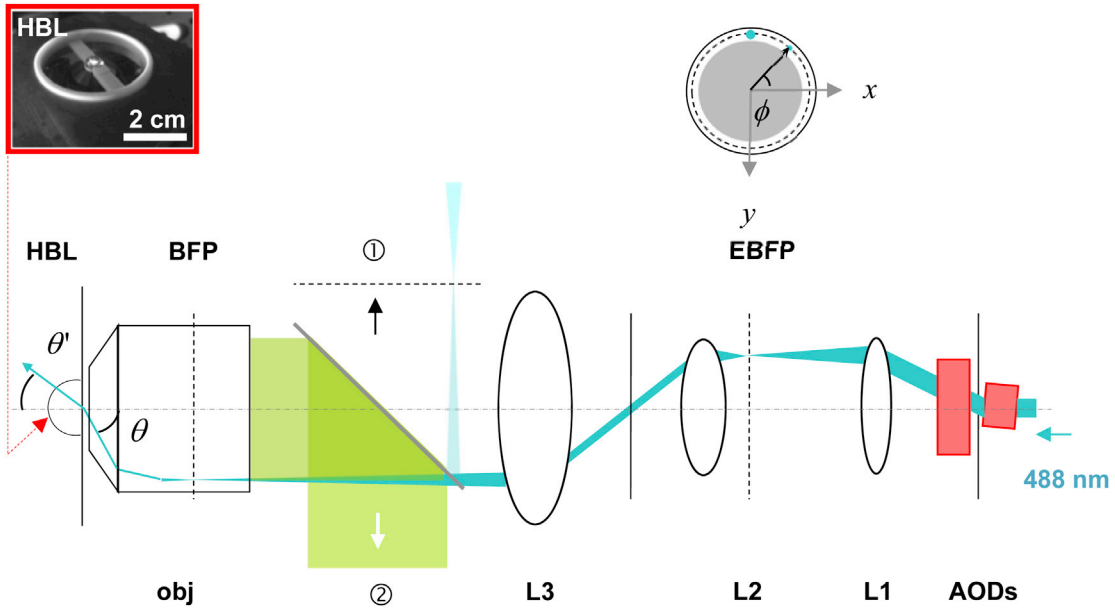

FIGURE 1 Simplified optical layout of the excitation optical path of our custom TIRF microscope. Solid and dashed lines designate conjugate field and aperture planes, respectively. Optical elements, obj: objective lens; BFP: back focal plane (*aperture plane*); L3: Rodagon focusing lens; L1, L2: compressing telescope that increases the scan angle; AODs: acoustooptical deflectors; EBFP: equivalent back focal plane. Insets show, on the left, a photograph of the half ball lens (HBL) in a custom holder on top of the objective that allowed us to measure beam angles otherwise obscured by TIR. Right, definition of variables in the objective BFP. r, dashed line – radius; ϕ azimuthal scan angle; gray area – radii below r_c corresponding subcritical angles (EPI); white annulus – radii corresponding to supercritical angles for which TIR occurs; turquoise spot is focused excitation beam (not to size); solid line – radius r_{NA} corresponding to limiting effective NA of the objective, NA_{eff}. To see this figure in color, go online.

indicated in the figure legends. We used low μW powers in the sample plane and integration times between 25 and 150 ms/frame (see Fig.S1).

Effective NAs of TIRF objectives (PlanApo ×60/NA1.45 oil TIRFM, APO N ×60/NA1.49 oil, both from Olympus, Hamburg, Germany; αPlan-Apochromat ×100/NA1.46oil, Zeiss, Oberkochen, Germany) were measured using a technique based on the detection of the supercritical-angle radiation pattern of near-interface dipoles (18). Mounting an additional Bertand lens for BFP imaging, we detected the fluorescence emitted by a thin layer of FITC (500 μM) spin-coated on a coverslip, Fig. S2.

AFM

Surface roughness of bare and treated BK-7 and quartz coverslips was measured with AFM (Bioscope, Veeco, Plainview, NY with Nanoscope IIIa controller). Surface roughness was calculated as $R_q = \sqrt{1/MN\sum_{j=1}^{M}\sum_{i=1}^{N} z^2(x_i, y_j)}$, $R_a = 1/MN\sum_{j=1}^{M}\sum_{i=1}^{N}\left|z(x_i, y_j)\right|$ or $R_t = \max(|z_{\max} - z_{\min}|)|_{\forall(x,y)}$. Here, M is the number of points per scan line and N is the number of lines, $z(x,y)$ is the vertical tip displacement at point (x,y). Tapping-mode AFM was used for wet coverslips.

Wavefront analysis

Phase aberrations were measured with a lateral shearing interferometric wavefront sensor (SID4, Phasics, Palaiseau, France). The beam parameter product M^2 and Strehl ratio $S = e^{-(2\pi\sigma/\lambda)^2}$ (σ being the root mean-square (RMS) deviation of the wave front and λ the wavelength) were calculated and plotted as a function of θ.

Image analysis

Fluorescence images were analyzed after subtraction of a dark image taken at the same exposure time, hardware- and EM-gain. Phase, beam-profile, dark-field, and objective-BFP images are shown as raw images. Dark-field and fluorescence images are displayed on an inverted (black-on-white) look-up table for better clarity in print with the intensity coded in an 8 bit gray value after autoscaling to image min-max, unless otherwise stated (gray scale sidebar). Image analysis was performed in METAMORPH (MDS Analytical Technology, Sunnyvale, CA), NIH ImageJ, and IGOR (Wavemetrics, Lake Oswego, OR).

For analyzing excitation directionality, circular line regions of interest were centered on the cell identified on bright-field (BF) images and the fluorescence intensity profile measured in negative staining plotted as a polar graph. We used $I(\phi)/I_{mean}$ to allow cell-to-cell comparison between experiments, and $CV = I_{SD}/I_{mean}$.

Weber contrast was calculated as $C_W = (I - I_b)/I_b$, where I and I_b are the fluorescence intensity of image features and background, respectively. I_b was measured in a large cell-free region of interest identified on the BF/fluorescence images. Signal intensities I were measured in regions of interest outlined by a border exceeding two times the SD of I_b. Michelson contrast (visibility) was calculated as $C_M = (I_{max} - I_{min})/(I_{max} + I_{min})$, RMS contrast as $C_{RMS} = \sqrt{1/MN\sum_{j=0}^{M}\sum_{i=0}^{N}(I_{ij} - \bar{I})^2}$, where I_{ij} is the intensity of pixel (i, j) of a $M \times N$ pixel image. $\bar{I}$ is the average fluorescence of all pixels.

Single lysosome intensities were measured on spTIRF and unidirectional TIRF images by fitting a Gaussian distribution with the single-spot intensity distribution and measuring peak and local background fluorescence.

Image segmentation and organelle-shape analysis was performed using METAMORPH's IMA tool. To isolate individual lysosomes or mitochondria the local background was suppressed by the subtraction of a corresponding low-pass filtered image (3.9 μm) and the result segmented using isodata histogram thresholding (19). In this procedure the image histogram is initially segmented into two parts using a starting threshold intensity $T_0 = 2^{B-1}$, half of the maximum dynamic range. The sample mean of the gray values associated with the foreground pixels ($m_{f,0}$) and the sample mean of the gray values associated with the background pixels ($m_{b,0}$) are then computed. A new threshold value θ_1 is computed as the average of these two sample means, $(m_{f,0} + m_{b,0})/2$. This process is repeated, based

upon the new threshold, until $T_k = (m_{f,k-1} + m_{b,k-1})/2$ converges, $T_k \rightarrow T_{k-1}$. Individual mitochondria were identified using {area $\geq$ 5 px (~1 μm^2) AND length $\geq$ 2 px (0.38 μm) AND breadth $\geq$ 2 px)} as a classifier. For each mitochondrion the area A (pixels above T_∞), orientation (angle between longest chord of the object and the horizontal, i.e., -90° = downward), shape factor ($\sigma = 4\pi A/P$, P = perimeter, i.e., flat = 0, …, 1 = circle), and elliptical form factor (ε = length/breadth) were measured. For the mitochondrial data set shown (imaged at 78° beam angle and 194-nm pixel size), T_∞ corresponded to 14.4 $\pm$ 2.8% (mean $\pm$ SD for $n = 24$ images) of the maximal intensity.

Similarity between fluorescence excitation patterns was assessed by taking 10 fluorescence images of a dilute FITC solution at one coverslip location (images A_n) before laterally displacing the coverslip by a controlled distance (images B_m, n, $m = 1,\ldots, 10$). Controlled lateral stage movements on different length-scales were produced with a piezo actuator and a micrometer screw, respectively. We then calculated, for every distance, the average image cross correlation $\langle A_n B_m \rangle$ for all permutations *nm*. The result was normalized with the average autocorrelation $\langle A_n A_m \rangle$, all *nm*.

Statistics

All measurements are reported as mean $\pm$ SD from at least three independent experiments (n reporting the total number of measurements). The means of normally and log-normally distributed data sets having the same variance were compared with Student's t-test. The nonparametric and distribution-free Kolmogorov-Smirnov-test was used for comparing nonnormally distributed data. All statistical operations used MATLAB (The MathWorks, Natick, MA) or IGOR. Points $\geq$1.5 $\times$ IQR above the third quartile or below the first quartile were considered as outliers (Turkey). Differences were considered significant for $p < 0.05$. On figures, *, **, and *** are shorthand for $p < 0.05$, $p < 0.01$, and $p < 0.001$, respectively, *n.s.* means not significant.

RESULTS

Beam spinning abolishes TIRF image nonuniformity but does not improve contrast

Optically dense organelles like mitochondria, lysosomes, secretory granules, or protein-rich cell adhesion sites inevitably scatter light. Irrelevant in epifluorescence, where the entire sample is illuminated, this scattering compromises the excitation confinement and flaws TIRF-based fluorimetry. In biological samples, most EW scattering occurs in forward direction, producing a flare of light in the sense of EW propagation (20,21). We used a custom-built variable angle (θ, ϕ) microscope incorporating a fast AOD-based beam scanner (14) to have full control of all beam parameters, Fig. 1. Negative staining (22) TIRFM images of unlabeled BON cells (having a morphology similar to a chromaffin cell) bathed in a fluorescein dextran-containing extracellular solution displayed irregular intensity bands colinear with the direction of EW propagation. Changing the azimuth ϕ at a constant polar angle θ rotated the EW propagation direction and also changed the stripe orientation. Maintaining θ constant while scanning ϕ at kHz frequency during image acquisition (14) produced a more evenly lit field of view, Fig. 2 *A*. Spinning reduced the coefficient of variation of the fluorescence intensity measured along a circular band around the cell ($CV = 0.12 \pm 0.05$ for spTIRFM vs. 0.31 $\pm$ 0.11 for unidirectional EW excitation, mean $\pm$ SD, $n = 4$), Fig. 2 *B*. See Fig. S1 for a detailed characterization of the AOD-based TIRF microscope.

A nonhomogeneous lit field-of-view adversely affects image quality and alters the conclusions drawn from TIRFM images. Fig. 3 compares TIRF images of the same cultured cortical astrocyte labeled with FM2-10, a lysosomal marker in this cell type (17), upon spinning and unidirectional EW excitation, respectively. Conventional TIRF images displayed directional features associated with the EW propagation direction that were absent from the corresponding spTIRF image, Fig. 3 *A*. Whole-image Weber (C_W) and Michelson contrast (C_M) were unaffected by beam spinning ($C_W = 13.6 \pm 3.4$ for unidirectional vs. 12.3 $\pm$ 3.6 for spTIRF; $C_M = 0.99 \pm 0.01$ vs. 0.99 $\pm$ 0.01, $n = 9$, *n.s.*) but more organelles were detectable with spTIRFM than with conventional EW illumination (66 $\pm$ 7 vs. 40 $\pm$ 16 spots; 0.018 $\pm$ 0.002 μm^{-2} vs. 0.010 $\pm$ 0.004 μm^{-2}; $n =$ 9 cells, $p < 0.01$). In line with this observation, individual fluorescently labeled lysosomes were brighter (4522 $\pm$ 1910 cts vs. 2871 $\pm$ 2750 cts, mean $\pm$ SD, $n = 21$, $p =$ 0.01) and their intensities were more uniform with spTIRFM than with unidirectional TIRFM ($CV = 42\%$ vs. 95%), for which organelles localized on or alongside the bright excitation bands had markedly distinct intensities, Fig. 3 *B*. Based on a single unidirectional TIRF image as that acquired with most commercial TIRF microscopes one would erroneously interpret such intensity differences as organelles being located at different axial distances, having unequal dye content, or different refractive index.

In addition to making intensity measurements more reliable, beam spinning abolished aberrant directional features that were observed when subcellular structures were aligned with the direction of EW propagation. For example, TIRFM images of astrocytes with fluorescently labeled mitochondria showed preferentially those mitochondrial chains aligned with the EW propagation direction, and beam spinning abolished this bias, Fig. 4.

Denser cell labeling, i.e., with fewer unlabeled regions, made the illumination nonuniformities of conventional TIRFM even more obvious, Fig. S3. In all cases, restoring the illumination symmetry produced images that more accurately portrayed the fluorophore distribution on the sample, improved the detectability of fluorescent organelles, and reduced the cell-to-cell variability. We conclude that spTIRFM facilitates the accurate quantification of biological processes at or near the plasma membrane. Aware of these advantages, we henceforth systematically used spTIRFM, unless it is explicitly stated.

Evanescent-wave scattering in the sample produces measurable far-field excitation

How much the cell itself is a contributor to nonevanescent excitation light? This is an important question for biological

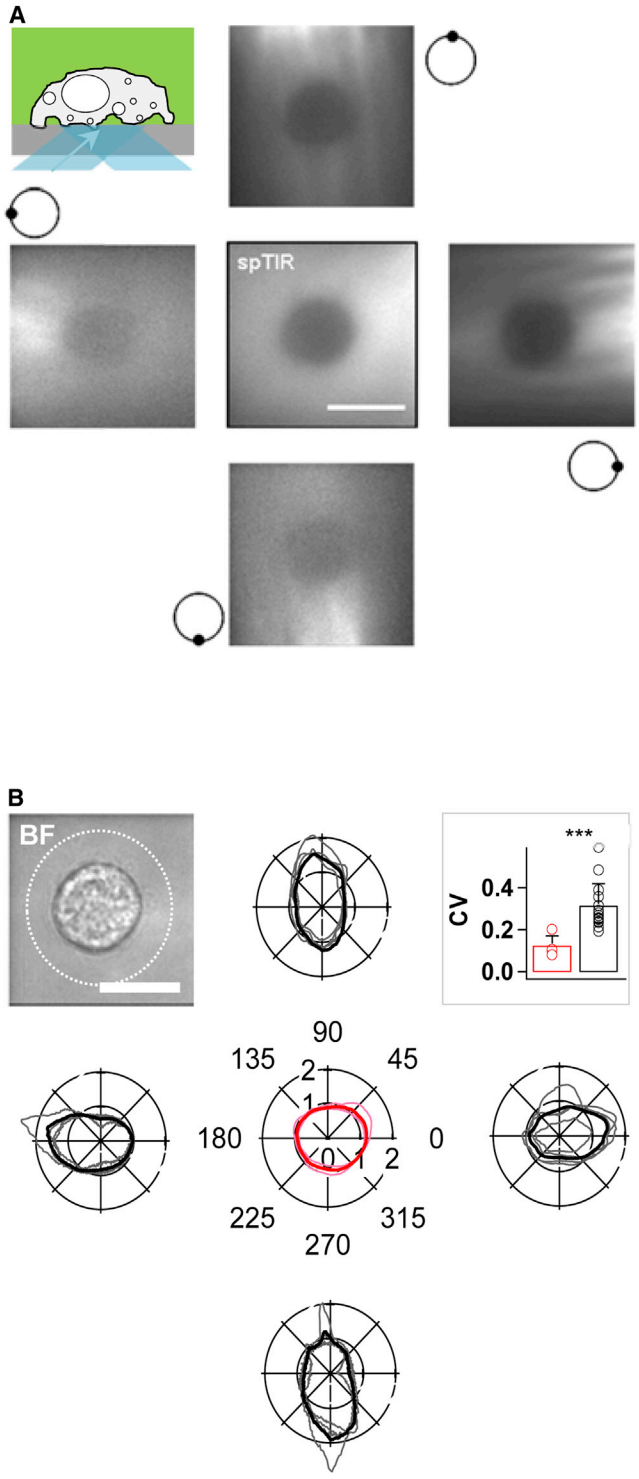

FIGURE 2 Azimuthal beam-scanning produces evenly lit TIRFM images. (*A*), negative-staining experiment: unidirectional and spTIRF (*center*) images of an unlabeled BON cell embedded in a fluorescein-dextran-containing extracellular saline. Contrast is inverted for clarity. Symbols indicate focused spot position in the objective BFP. Note excitation patterns colinear with evanescent-wave (EW) propagation direction. Azimuthal beam spinning evens out excitation nonuniformities. Polar beam angle θ was 68°. Scale bar, 10 μm. (*B*) Evolution of fluorescence intensity along a 2-μm wide circular region (*indicated on the bright-field image*, BF) for different EW propagation directions and spTIRF. Gray lines are individual measurements from $n = 4$ cells, black trace is their ensemble average. Inset shows reduction of the coefficient of variation (CV) of the measured intensity with spTIRF (0.12 ± 0.05), red, compared to unidirectional TIRFM (*black*, 0.39 ± 0.15, 0.29 ± 0.05, 0.27 ± 0.03, 0.28 ± 0.14, respectively, for NWSE cardinal images. 0.31 ± 0.11 is the mean ± SD over all unidirectional TIRF images, $p < 0.001$ vs. spTIRF). Objective was ×60/1.45NA. To see this figure in color, go online.

TIRF microscopy because calibration measurements are generally made with beads or fluorescent filaments in cell-free solution and are then extrapolated to quantify and interpret intracellular fluorescence. If significant, cell-induced scattering would also invalidate the assumption of shift invariance, i.e., the comparability of intensities recorded at different subcellular locations.

If the excitation nonuniformities observed in Figs. 2, 3, and 4 were primarily sample-induced then the fluorescence measured in a circular band around a nonlabeled BON cell embedded in fluorescein-dextran containing solution should be higher than that recorded in the same place on a cell-free control area. Furthermore, we would expect the cell-induced contaminating fluorescence to increase when increasing the EW penetration depths $\delta(\theta)$, because larger penetration depth enlarge the light-cell interaction volume and should thus favor EW scattering. To test these hypotheses, we systematically varied θ while continuously scanning ϕ. Fig. 5 *A* shows the resulting fluorescence profiles, measured across the image diagonal in the presence and absence of a BON cell, respectively. The image center, where the basal plasma membrane makes close contact with the coverslip, partially excludes the dye (20) and hence fluoresces less than the same region on the cell-free control image—even for very shallow penetration depths ($\theta = 75°$, calculated $\delta = 63$ nm). On the contrary, the fluorescence measured close to the cell boundary (detected on the BF image) was increased compared to the cell-free case and grew further with distance, as if part of the illumination was propagating and increasingly reaching out to larger depths beyond the cell/substrate interface, Fig. 5 *B*.

We recorded such intensity profiles at different penetration depths $\delta(\theta)$ and normalized them with the profiles measured at the same θ in control, Fig. 5 *C*. At shallow penetration depths, the fluorescence close to the cell was twice as high as that measured in the cell-free case. However, contrary to what we expected, this extracellular signal was not proportional to the probe depth and was even relatively less important at larger (calculated) penetration depths of $\delta = 71$, 84, and 108 nm, than at 63 nm. In fact, when we corrected the fluorescence $F(\theta)$ measured in a ring region around the cell for the θ-dependence of the EW intensity $I_0(\theta)$ itself (using the fluorescence of the thin dye layer underneath the cell as a reference, see Fig. S4 for the limits of this approximation), we found that the normalized intensity $[F_s'(\theta)]_{norm}$ only slightly depended on the penetration depth. Instead, it was dominated by a large angle and penetration depth-independent offset, Fig. 5 *D*.

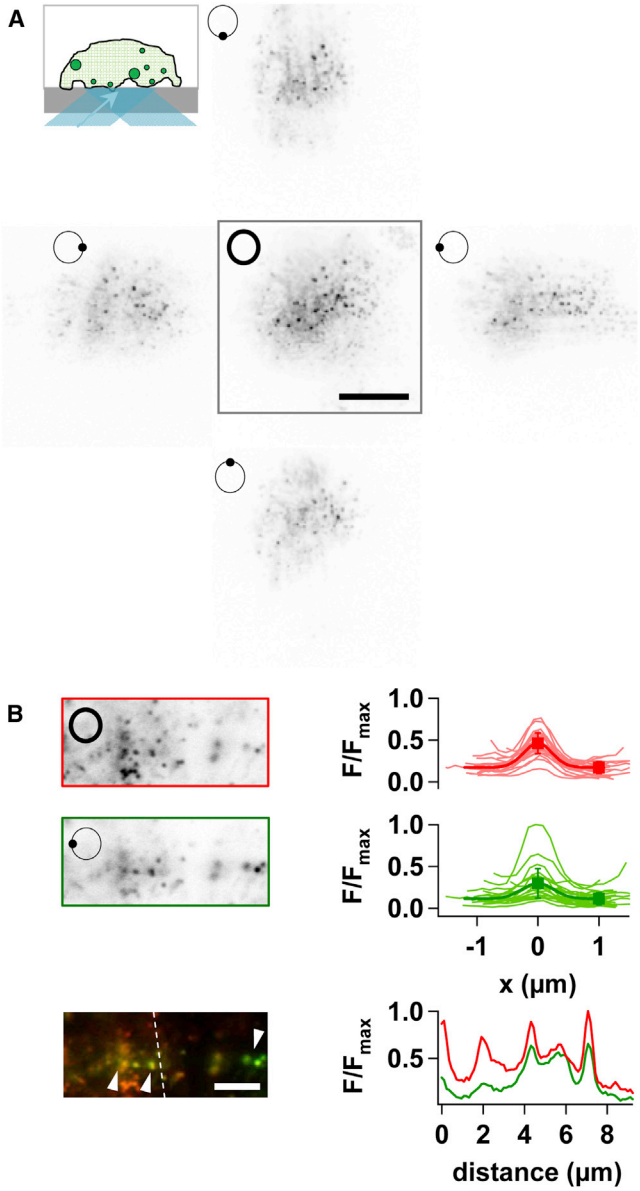

FIGURE 3 Uneven illumination affects the interpretation of biological TIRF images. (*A*) Unidirectional and spTIRF images of fluorescent lysosomes in a cultured mouse cortical astrocyte labeled with FM2-10 (see (17)) $\theta = 73°$. Symbols are the same as in Fig.2. Note the flare of intracellular fluorescence collinear with EW propagation direction, which is absent on the spTIRF image. Scale bar, 20 μm. (*B*) Left, zoom on an image region from a spTIRF (*top*) and unidirectional image (*middle*) and their pseudocolor overlay (*bottom*). Arrowheads point on excitation light propagating across the image. $\theta = 70°$, scale bar, 5 μm. Right, single-lysosome intensity profiles (*light traces*) upon spTIRF (*red*) and unidirectional (*green*) excitation and their mean $\pm$ SD peak and local background (*solid trace* and *symbols*), $n = 21$. Bottom, cross-sectional intensity profile along the dashed line in panel *B*. Objective was $\times$60/1.45NA. To see this figure in color, go online.

Taken together, we conclude that EW scattering by the sample converts confined light into propagating light that is readily detected in negative staining experiments. Yet, the measured far-field excitation only weakly depends on this sample-induced scattering, suggesting that the light impinging at the cell was already containing propagating components. We next asked where these effects could come from.

Evanescent-wave scattering at the coverslip surface is minor

Perhaps, not volume scattering in the sample but scattering at the surface of the reflecting interface is dominant. Evidence for the importance of surface roughness in perturbing the EW comes from the observation of nonspecular reflections of slow atoms in EW mirrors that were abolished by flame polishing (23). We used scanning AFM to evaluate the roughness of commercial borosilicate and fused silica coverslips. Bare BK-7 coverslips revealed scratches, dimples, and holes on some, but no obvious surface defects on other coverslips from the same batch; quartz had a characteristic crystalline rolling hill aspect, Fig. 6 *A*. Rejecting the outliers, we found for the remainder of bare coverslips a subnanometric RMS roughness (R_q), Table 1. These height variations doubled upon poly-ornithine or collagen treatment (Fig. 6 *B*) but they were still $<$1 nm. R_q increased to ~2 nm when wetting the coated coverslips with physiological saline. However, these average values concealed that the peak roughness R_p was now of the order of tens of nanometers, and peak-to-peak heights locally reached 60 nm for larger collagen aggregates. Thus, once hydrated, cell adhesion molecules can produce height features having a size of the order of the EW penetration depth.

If such irregularities led to a significant EW scattering, one would expect them to disrupt TIR locally, as it is observed in the case of EW scattering at a Mie particle (24,25). We first confirmed that we could detect EW scattering produced by individual nonfluorescent 2.8-μm diameter latex beads, Fig. 6 *C* ($dF/F_0 = 0.03 \pm 0.02$, $n = 11$, $\theta = 68°$, $\lambda = 488$ nm). However, no such intensity fluorescence increase due to forward EW scattering was detectable on collagen-coated coverslips (not shown). In fact, local excitation nonuniformities seemed to be dominated by other factors: neither did collagen treatment appreciably modify the excitation pattern observed in fluorescein solution, nor were they sensitive to lateral coverslip movement (Fig. 6 *D*), nor did they appreciably vary from one coverslip to the other (not shown). Thus, most of the excitation inhomogeneity was neither the result of EW volume nor surface scattering, as if another far-field excitation component unrelated to EW scattering was present. Such long-range excitation was reported earlier in experiments using index-matched fluorescent beads to probe the axial intensity decay of the EW (12). Perhaps, this propagating excitation light originates far from the sample plane, inside the microscope. This premise was supported by the observation that negative-staining fluorescence images taken

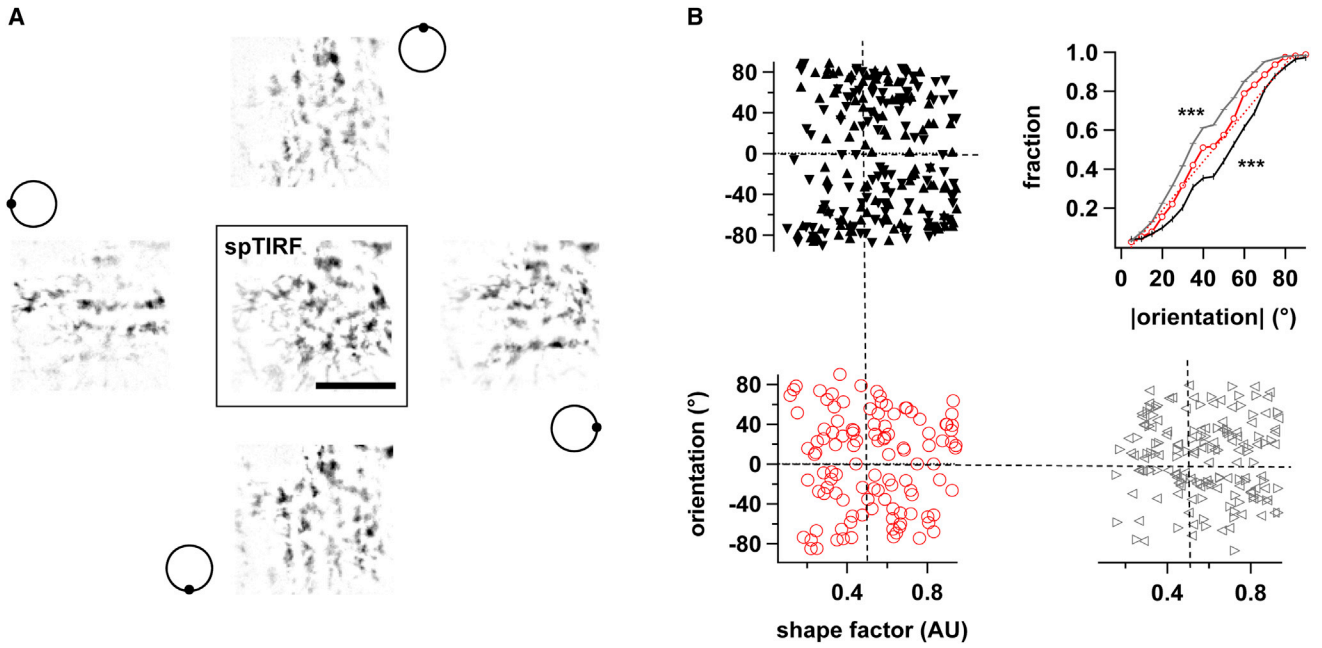

FIGURE 4 Conventional eccentric-spot TIRF excitation introduces a directional detection bias. (*A*) Unidirectional TIRFM images of a cultured cortical mouse astrocyte expressing enhanced green fluorescent protein linked to a mitochondrial targeting sequence (mito-GFP) show preferentially those mitochondria that are aligned parallel to the EW propagation direction, whereas those perpendicular to it are less visible. The center image upon azimuthal beam spinning (spTIRF) seems less biased. Scale bar, 10 μm, contrast inverted for clarity in print. (*B*) Quantitative morphometry confirms that mitochondria detected upon illumination with a horizontally propagating EW (*gray open triangles*) had, on average, orientations closer to the horizontal axis, (33.7° ± 16.6°, median ± abs. deviation, 268 mitochondria in $n = 6$ cells), whereas those detected with a 90°-rotated EW field (*black solid triangles*) were orientated closer to the vertical axis (53.2° ± 18.6°, 357 mitochondria in $n = 6$ cells, $p < 0.001$), as if mitochondria acted as light guides. Triangles point in the direction of EW propagation. Restoring a rotationally symmetric illumination by azimuthal beam scanning abolished the directional detection bias (*red circles*), and the cumulative distribution of absolute orientations (between 0° and 90°) now had a median at the expected 45° ($p < 0.001$ versus each of the four unidirectional images, 155 mitochondria in $n = 6$ cells). Color coded as on panels showing orientation versus shape factor that is $4\pi A/P^2$, where A and P are the organelle area and perimeter, respectively. To see this figure in color, go online.

with the same objective in the presence and absence of a cell showed strikingly similar overall patterns, Fig. 6 *E*, and that distinct characteristic excitation patterns were associated with each objective, Fig. 6 *F*. Excluding the coverslip surface as a major source for unwanted stray-excitation, we next investigated the role of the microscope illumination optics in generating nonevanescent excitation light.

Objective glare and aberrations of peripheral beams limit excitation confinement

Because its excitation and emission optical paths share common elements, objective-type TIRF is known to have a lower signal/background ratio than prism-based TIRF (26,27). The optical surfaces of the many lenses inside the high-NA objective have been invoked as one source of stray excitation. Another possible origin of stray light is the extreme off-axis beam propagation required for TIRF: to hit the reflecting interface at supercritical angles, light travels through the very objective periphery where aberration corrections of common high-NA objective designs are known to fail (28).

To quantify the amount of far-field excitation light at the same time as the TIRF intensity, we used a dark-field detection scheme: a ×20/NA0.8 air objective was positioned above the coverslip surface and scattered excitation light collected within the objective's NA imaged onto a small CCD camera. We measured the scattered-light intensity I_s as a function of θ and used the autofluorescence generated in a small collagen clump at the surface of the coverslip as a readout of TIRF and hence the local intensity $I_0(\theta)$, Fig. 7 *A*. As expected from theory, we recognized in the fluorescence trace the critical angle θ_c as an intensity peak close to its calculated value. Likewise, a sharp intensity cutoff was observed close to the limiting angle θ_{NA} corresponding to the nominal objective NA. The dark-field intensity $I_s(\theta)$ followed $I_0(\theta)$ for small angles but then deviated and sharply increased beyond 69°, well before the limiting θ_{NA}~74°, as if significantly more propagating excitation light was produced at such high beam angles. If this stray light resulted from a clipping of the marginal rays by the objective boundary or from the breakdown of aberration corrections at high NAs, this should manifest as a change in the beam shape. We therefore wanted to directly measure the beam profile as a

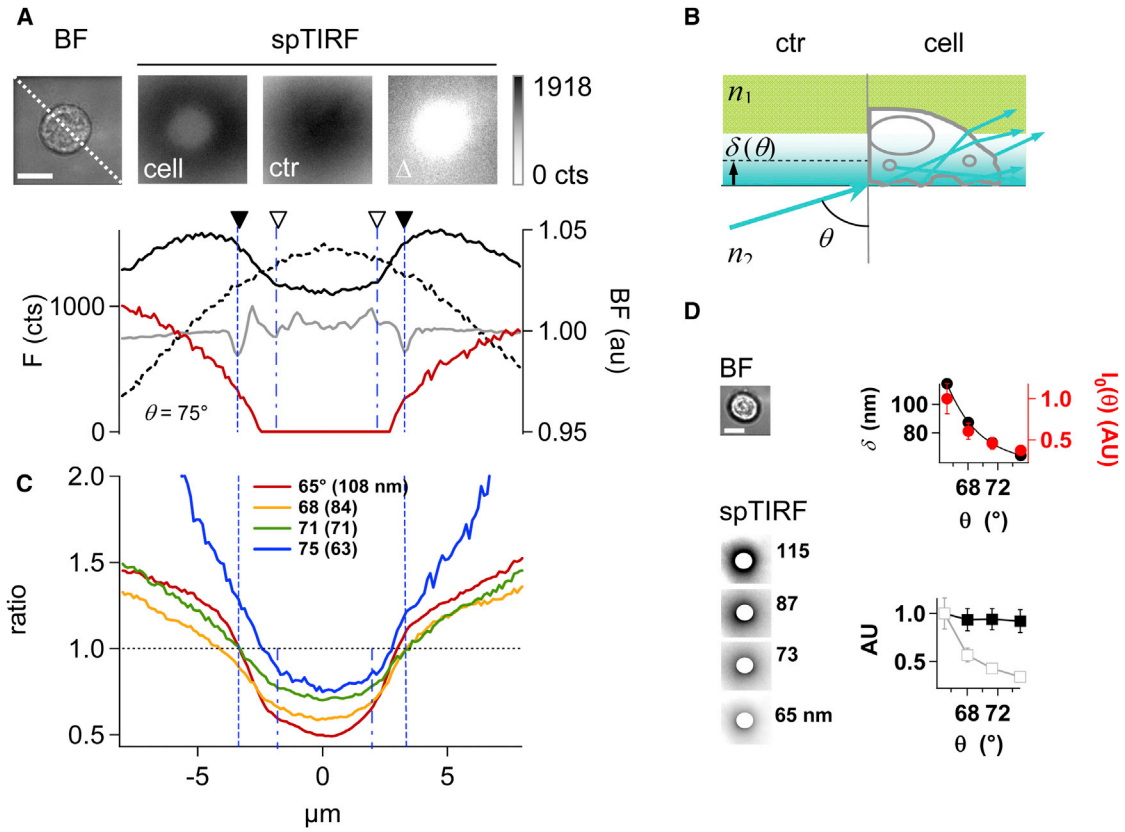

FIGURE 5 Cell-induced EW scattering is detectable but not the dominant source of propagating background excitation. (*A*) Top, BF and spTIRF images of an unlabeled BON cell embedded in fluorescence dextran, along with a cell-free control image taken nearby on the same coverslip (ctr), and their difference image (marked Δ). $\theta = 75°$. Scale bar, 10 μm. Bottom, cross-sectional intensity profiles (measured over a 1-μm wide line region) along the image diagonal shown. Solid and open arrowheads identify plasma membrane and adhesion footprint detected from the BF and spTIRF image, respectively. Black traces are fluorescence intensity profiles in the presence (*solid*) and absence (*dashed*) of the cell, red is difference trace. (*B*) Sketch of how anisotropic scattering at dense intracellular organelles generates propagating excitation light detectable in the far field. (*C*) Relative fluorescence intensity profiles. Profiles measured the presence of the cell were normalized with the cell-free intensity, for different angles θ (*color coded*). Numbers in brackets give calculated penetration depths $\delta(\theta)$. Note the partial exclusion of dye from the cell adhesion site (ratio <1) and the extra signal compared to the cell-free case (ratio >1) around the cell. For $\theta = 75°$ at 5-μm distance from the cell the average fluorescence was roughly twice that measured for a bare glass/fluorescein interface. (*D*) Left, BF and spTIRF negative-staining fluorescence images of an unlabeled BON cell at different penetration depths. Footprint region blocked out for clarity in display. Right, θ-dependence of the calculated EW penetration depth $\delta(\theta)$ (*black*) and measured EW intensity $I_0(\theta)$ (*red*). Bottom, θ-dependence of the scattered fluorescence intensity measured in a ring around the cell before (*open symbols*) and after normalization with $I_0(\theta)$ (*solid symbols*). Mean ± SD, $n = 5$ cells. AU = arbitrary units. Objective was ×60/1.49NA. To see this figure in color, go online.

function of θ. One possibility would have been to image the totally reflected beam onto a camera, but this beam passes twice through the objective and therefore might represent an overestimate of objective-induced wavefront aberrations.

To diagnose the beam at angles θ otherwise obscured by TIR, we carefully positioned an oil-coupled high-index solid immersion lens on top of the TIRF objective (see *inset* in Fig. 1), allowing to image the now transmitted beam onto a commercial wavefront analyzer. We then calculated the beam parameter product (M^2) and Strehl ratio as a function of θ. Two objectives from different manufacturers performed well up to θ ~50° but thereafter, the beam quality gradually decreased significantly, Fig. 7 *B*.

Both the increase in stray light and the wavefront aberrations observed at high beam angles could be explained if the objectives were not quite as good as claimed by the manufacturers. To exclude that objectives had an effective NA (NA_{eff}) smaller than specified (a finding reported in the 1990s for some of the then available 1.4-NA objectives that had true NAs closer to 1.38) we measured NA_{eff} using a technique based on supercritical angle fluorescence detection (18). Our measurements indicate that most of the NA1.45–1.46 objectives generally fulfilled their specifications, but a nominal 1.49-NA lens only had a NA_{eff} = 1.47, Fig. S2.

Taken together, our data suggest that off-axis aberrations and vignetting degrade objective performance at the high NAs required for TIRF microscopy. The objective is a non-negligible source of unwanted far-field excitation light. Its contribution to nonevanescent excitation light is unaffected by beam spinning and causes unwanted far-field excitation

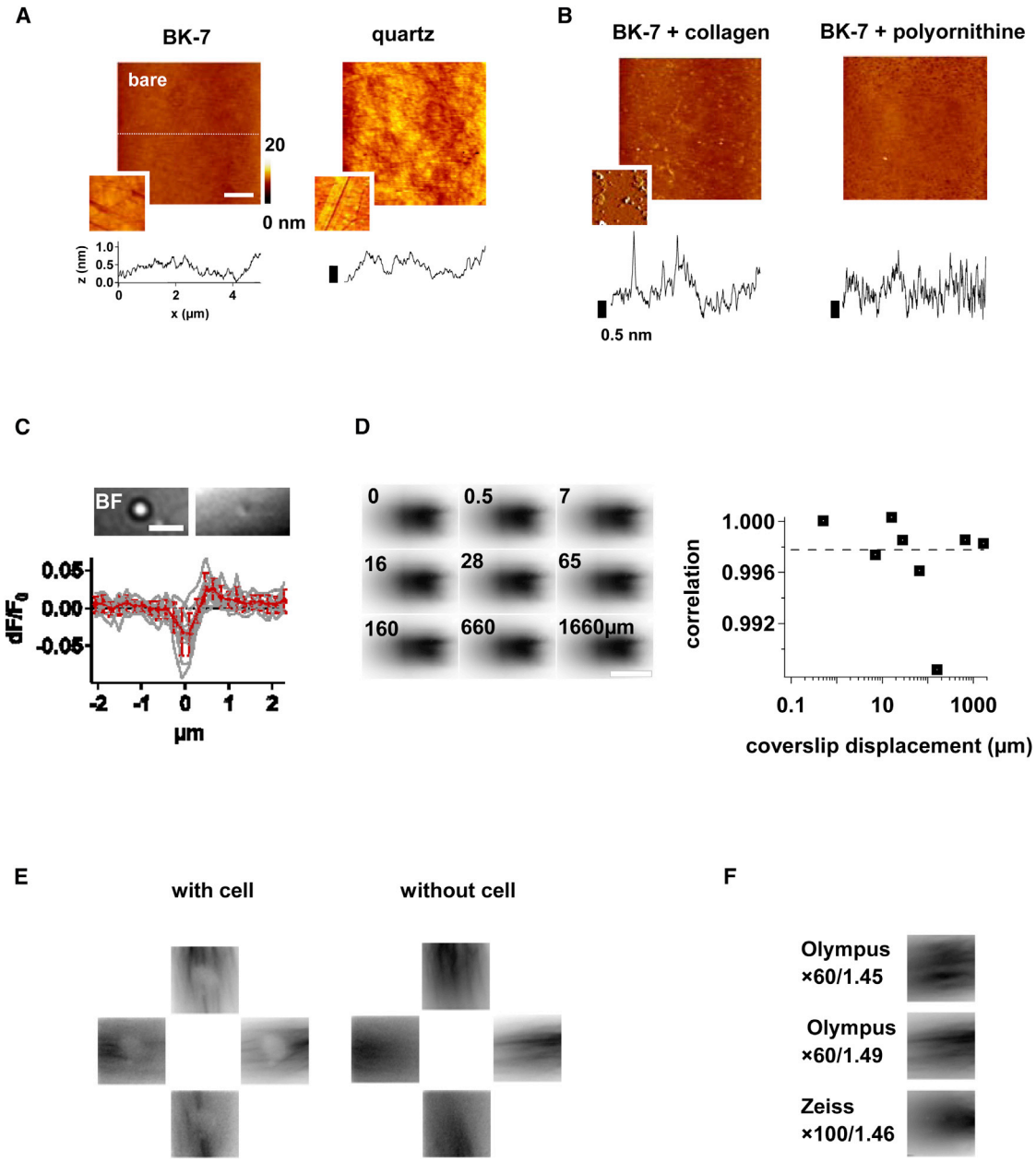

FIGURE 6 Instrument-induced stray light rather than local EW scattering at the coverslip surface dominate excitation nonuniformities. (A) Top, representative contact-mode AFM images of bare borosilicate (BK-7) and fused silica (quartz) coverslip surfaces. Pseudocolor height scale, 0–20 nm. RMS roughness R_q for images shown is 0.43 and 0.58 nm, respectively. Insets, examples of coverslips that displayed scratches and surface defects and that were rejected from analysis. Bottom, surface profiles taken along the dotted line indicated. (*B*) Same after collagen (*left*) or polyornithine treatment (*right*). $R_q = 0.49$ and 0.38, respectively. Color code and profile scale as in (*A*). Inset, tapping-mode image of wet collagen-coated coverslip. Scale is 0–20 nm for images but 0–200 nm for inset. See Table 1 for quantifications. (*C*) Top, BF and unidirectional TIRF image of a 2.8-μm diameter nonfluorescent latex bead embedded in FITC dextran. Bottom, normalized (dF/F_0) intensity profiles (*gray*) and population average (*red*) along a line region across the bead. F_0 is the unperturbed fluorescence nearby. (*D*) Left, unidirectional TIRF excitation patterns in a dilute fluorescein solution ($\theta = 64°$, objective ×60/1.45). Bar, 50 μm. Right, measured fluorescence patterns were insensitive against lateral coverslip displacement. Average image cross correlation amplitude (normalized to the autocorrelation amplitude at zero offset) between 10 original images and 10 images taken after lateral displacement of the coverslip. Dotted line, linear fit 0.997 ± 0.002. (*E*) Comparison of uneven illumination patterns upon unidirectional EW excitation in the presence of a BON cell (*left*) and a cell-free control region on the same close by (*right*). Note the overall similarity of the patterns. (*F*) Characteristic fingerprints of three different high-NA objectives. To see this figure in color, go online.

compromising the interpretation of spTIRF images. The following companion work explores the related topic of instrument stray light generated further downstream along the microscope optical path, as well as a strategy for efficiently rejecting fluorescence generated by propagating excitation light.

TABLE 1 Coverslip surface roughness measured with AFM

	BK-7		Quartz	
	Bare, dry		Bare, dry	
R_q (nm)[a]	0.24 ± 0.04 ($n = 8$)		0.37 ± 0.05 ($n = 4$)	
	Polyornithine, dry	Collagen, dry	Polyornithine, dry	Collagen, dry
R_q (nm)[a]	0.44 ± 0.12 ($n = 5$)	0.44 ± 0.27 ($n = 5$)	0.65 ± 0.31 ($n = 6$)	0.69 ± 0.06 ($n = 4$)
	Polyornithine, wet		Polyornithine, wet	Collagen, wet
R_q (nm)[a]	5.4 ± 2.2 ($n = 10$)		2.8 ± 1.2 ($n = 5$)	2.6 ± 0.3 ($n = 5$)
R_q (nm)[b]	1.4 ± 0.5		2.8 ± 1.2	2.0 ± 0.4
R_a (nm)[b]	1.0 ± 0.3		1.6 ± 0.8	1.1 ± 0.2
R_t (nm)[b]	24.1 ± 8.4		27.8 ± 14.6	49.8 ± 9.1
pk-pk height (nm)[b]	16 (min); 60 (max)		13 (min); 48 (max)	41 (min); 62 (max)

[a]RMS roughness over 5 μm × 5 μm of nonselected commercial coverslips.
[b]RMS and absolute roughness as well as peak height, calculated over 2 μm × 2 μm regions of interest from selected coverslips devoid of large surface defects.

DISCUSSION

spTIRF is no cure-all against nonevanescent excitation light

Single-eccentric spot laser excitation of TIRF generates interference fringes, forward EW scattering, and shadowing by optically dense organelles that produce an uneven illumination across the field of view (7,9,12–16,20,21,24,25). The direct illustration of this phenomenon is that TIRF images change when the EW propagation direction is altered (Figs. 2, 3, 4 and Fig. S3). In the past, two strategies have been explored for obtaining a more accurate representation of the near-membrane fluorophore distribution: nonlinear EW excitation, and azimuthal beam spinning.

Analogous to scanning-type two-photon excitation fluorescence (2PEF) microscopy, femtosecond (fs)-pulsed EW excitation reduces nonevanescent background excitation because scattered photons are too dilute to generate appreciable fluorescence (21,29–31). Although effective, 2PEF TIR has, in fact, rarely been used. This is probably due to the need for an expensive fs-pulsed light source, laser safety issues, and the often higher two-photon photo damage. Furthermore, as the laser beam must be focused in the objective BFP, the illumination scheme inherent to objective-type TIRF produces high instantaneous peak powers in the BFP inside the objective lens that can easily reach or exceed the objective damage threshold (21,29). Lower laser powers or less tight focusing, in turn, reduce the field-of-view over which 2PEF can be generated, spread the beam angle and penetration depth, and thereby diminish the advantages scanningless full-field imaging. Of note, shaped 10-fs pulses have recently been shown to produce large-field EW excitation over ~100 × 100 μm^2 (30).

The second, alternative technique is based on beam-scanning and one-photon excitation (13–16). Rapidly and continuously changing the EW propagation direction during image acquisition produces a more uniform illumination by averaging over excitation nonhomogeneities and avoids shadowing by dense objects in the sample. Unlike two-photon TIRF, beam scanning spatially redistributes scattered photons, but it does not fundamentally address the problem of diffuse fluorescence generation by nonevanescent excitation light. Conceptually, two-photon and spTIRFM are analogous to similar approaches used to improve optical sectioning and obtain more evenly lit images in selective-plane illumination microscopy (32) and highly inclined laminar optical sheet imaging (14,33), which share with TIRFM the principle of excitation confinement. Different spTIRF implementations have been proposed, using a rotating wedge, mirror- or AOD-based scanners. A recent study pointed out its benefits for fluorescence resonance energy transfer quantification (16). However, a rigorous evaluation of how beam scanning affects TIRF image quality has been missing. Our systematic comparison of unidirectional versus spTIRF images at different penetration depths and for various fluorescent labels shows that spTIRFM abolishes the effects of anisotropic scattering and is superior to conventional TIRFM in a broad range of experimental conditions. Nevertheless, beam spinning is no cure-all. Neither does it improve image contrast (Figs. 3 and 4), nor does it abolish the unwanted far-field excitation associated with objective-type TIRFM (Figs. 5 and 7).

Both instrument glare and EW scattering contribute to far-field excitation

In TIRF experiments, it is desirable to correlate intensity with fluorophore axial position or concentration. That the quantitation of TIRF intensities is not so straightforward has been pointed out (6–9) but only a few studies tried to account for EW scattering (21,29,34). This is a surprise, because it has been known for long that cells scatter evanescent light that is then detectable in the dark field: in 1956 Ambrose used prism-based dark-field surface contact microscopy to study cell motility and migration on glass surfaces (35,36). Our study corroborates and extends the observations of this classical work to the now currently used objective-type TIRF geometry. Of importance,, in this prismless geometry cell-induced EW scattering, albeit detectable, it is not the largest contributor to propagating excitation light, which for many practical biological TIRF experiments (moderate beam angles and labeling density

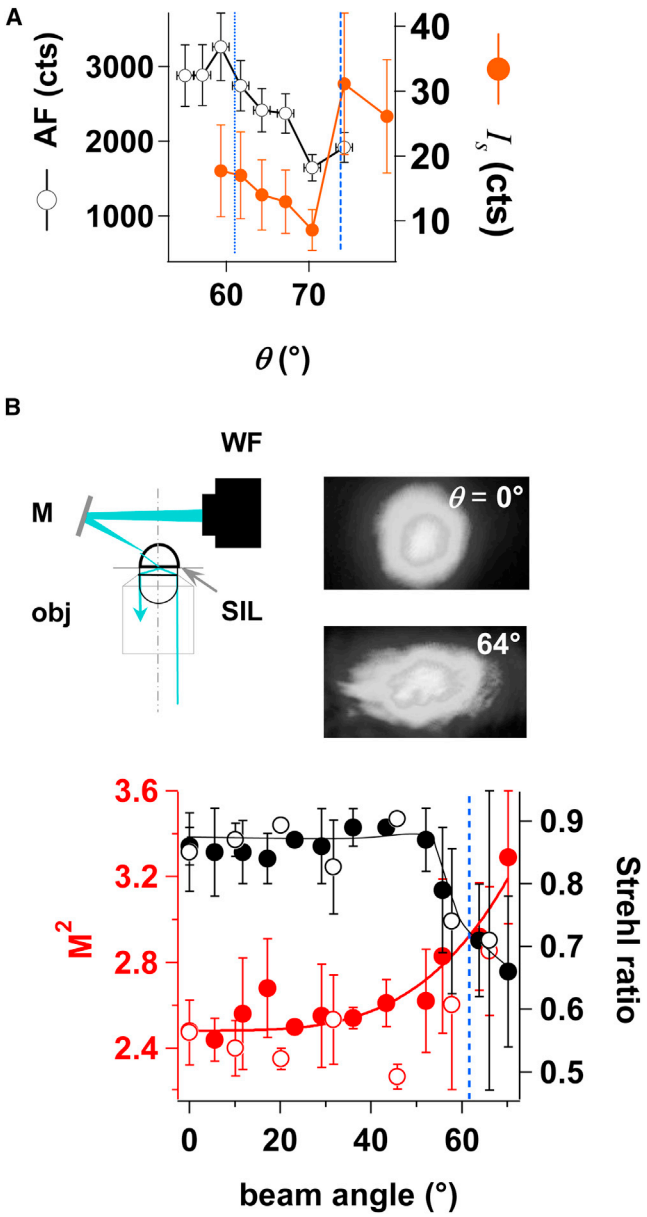

FIGURE 7 Off-axis aberrations and scattering inside the objective lens contribute to the loss of excitation confinement. (*A*) Evolution with beam angle θ of the autofluorescence (AF) of a small collagen clump on the coverslip surface and of the far-field excitation light detected through a ×60/NA1.1 dipping objective in a dark-field geometry (I_s). Dotted and dashed blue lines are the critical angle (~61°) and limiting NA (~74°) of the TIRF objective, respectively. Note the sharp increase in scattered light close to the objective NA. (*B*) Wavefront analysis of the laser beam impinging at the reflecting interface as a function of θ. Top left, optical layout used for wave-front measurements. obj: TIRF objective, M: mirror, WFA: wavefront analyzer. Right, intensity images taken with the laser beam on axis (0°) and beyond the critical angle (64°). M^2 and Strehl ratio were of 2.5 and 0.8 (3 and 0.6) at $\theta = 0°$ (64°), respectively. Bottom, evolution of M^2 (*red*) and Strehl ratio (*black*) with θ, for a ×60/NA1.45 (*dots*) and ×100/NA1.46-objective (*circles*). Mean ± SD from triplicate measurements. Note the degradation of beam quality already below θ_c. To see this figure in color, go online.

as well as weakly scattering samples) will be objective- and instrument-generated stray light. This is plausible, as several authors have previously reported a lower background and crisper TIRF images for prism- compared to objective-type TIRFM. The inferior performance of objective-type TIRF has been attributed to higher stray reflections inside the objective, interference of partially reflected beams, or propagating shafts of light emerging from the margin of the objective. Moerner and colleagues (37) estimated that as little as 26% of the initial power was returned from the objective in the totally reflected beam which, taking into account typical objective transmissions of ~80–90% in the visible, suggests important stray losses along the excitation optical path ($0.8^2 \gg 0.26$).

We find here that only a fraction of propagating excitation light observed in objective-type TIRF results from EW scattering in the sample (Figs. 2–5) or at irregularities of the reflecting interface (Fig. 6). Instead, an important part of stray excitation is angle- and sample-invariant, but it depends on where the excitation laser beam travels through the microscope objective. Thus, stray light is inherent to the illumination scheme used in prismless TIRF. Interestingly, variable-angle dark-field and TIRF imaging revealed an abrupt increase in glare for beams passing close to the objective periphery. This enhancement was accompanied by an increase in wavefront aberrations of high-NA beams (Fig. 7). With minor differences, all three high-NA objectives used in this study behaved similarly. Thus, at least for the marginal rays, common high-NA objective designs seem to operate close to or at the limits of their design specifications (28). Our study also underpins the importance of testing high-NA objectives individually: nominally identical objectives differed slightly and not all objectives met their specifications, suggesting that the commercial race to ever higher NAs has led to somewhat overly optimistic statements of optical performance.

Furthermore, upon 488-nm excitation with low μW power and EMCCD detection, all three tested objectives displayed measurable yellow-green autofluorescence (Fig. S2). This instrument fluorescence passes undetected as a background offset when imaging the sample-plane. BFP imaging with a Bertrand lens allowed us to identify the origin of this fluorescence inside the objective. Equivalent back focal plane imaging, on the excitation (14) as on the emission site, is a powerful tool facilitating the alignment and helping to understand and control instrument limitations.

Finally, in using spTIRFM, we identified an unexpected source of variability among TIRF experiments: the steep dependence of the EW intensity $I_0(\theta)$ and of the penetration depth $\delta(\theta)$ on the incidence angle make unidirectional TIRF extremely sensitive to even the slightest coverslip tilt. Such tilt can result from mechanical strain in the sample holder or manufacturing tolerance between the coverslip holder and microscope stage and is only seen when the sample is illuminated from several angles.

CONCLUSION

Most published TIRF data are based on experiments using unidirectional EW excitation. This type of illumination is particularly sensitive to objective- and cell-induced illumination nonuniformity. For angles close to the critical angle, the excitation confinement is disrupted locally at high-index organelles, creating intense beamlets along the original EW propagation direction. Strong absorbers result in shadowing. It would thereby seem important to study only those organelles in unidirectional TIRF (e.g., secretory granules) that are on the up beam side of cells that themselves are not in the perturbed field produced by other cells even farther up beam. Our study demonstrates that spTIRF offers an elegant but only partial solution to this problem by spatially averaging over directional features. However, it does not abolish the fluorescence generated by unwanted far-field excitation, which in large part originates inside the illumination optical path of the TIRF microscope and for the rejection of which other strategies need to be developed.

SUPPORTING MATERIAL

Four figures, three tables, methods, list of abbreviations, and references (38–45) are available at http://www.biophysj.org/biophysj/supplemental/S0006-3495(14)00079-4.

AUTHOR CONTRIBUTIONS

M.B. and M.O. conceived and built the microscope, M.B., K. H., M.O., C. T. and M.T. performed experiments, M.B and M.O analyzed data. M.O. designed and supervised research and wrote the manuscript.

The authors declare no conflicting interest.

We thank Isabelle Fanget and Cécile Debaecker for BON cell culture, Dongdong Li and Cathie Ventalon for help with experiments, Patrice Jegouzo for custom mechanics and Valentina Emiliani (CNRS UMR8154), Sven Konzack (Olympus) and Gérard Louis (Paris Descartes) for the loan of equipment. We thank Frank Lison (TILL Photonics), Christian Seebacher, and Rainer Uhl (both LMU Munich) for helpful discussions, Marcel Lauterbach for commenting on an earlier version of the manuscript, and Jac Sue Kehoe (CNRS UMR 8118) for careful proofreading.

This work was supported by the European Union (FP6-STRP-No. 037897-AUTOSCREEN, FP7-ERA-NET No. 006-03-NANOSYN), the *Agence Nationale de la Recherche* (ANR P3N 09-044-02 nanoFRET^2), the FranceBioImaging (FBI) initiative and mobility support from the Franco-Bavarian University Cooperation Centre (BFHZ-CCUFB). AFM imaging was performed on the Paris Descartes St Pères core imaging facility, *Service Commun de Micro-scopie* (SCM). The Oheim lab is part of the École des Neurosciences de Paris Ile-de-France (ENP) network and the C'nano Ile-de-France nanoscience and nanotechnology excellence cluster.

REFERENCES

1. Chung, E., D. Kim, and P. T. So. 2006. Extended resolution wide-field optical imaging: objective-launched standing-wave total internal reflection fluorescence microscopy. *Opt. Lett.* 31:945–947.
2. Gliko, O., G. D. Reddy, …, P. Saggau. 2006. Standing wave total internal reflection fluorescence microscopy to measure the size of nanostructures in living cells. *J. Biomed. Opt.* 11:064013.
3. Kner, P., B. B. Chhun, …, M. G. Gustafsson. 2009. Super-resolution video microscopy of live cells by structured illumination. *Nat. Methods.* 6:339–342.
4. Gould, T. J., J. R. Myers, and J. Bewersdorf. 2011. Total internal reflection STED microscopy. *Opt. Express.* 19:13351–13357.
5. Leutenegger, M., C. Ringemann, …, C. Eggeling. 2012. Fluorescence correlation spectroscopy with a total internal reflection fluorescence STED microscope (TIRF-STED-FCS). *Opt. Express.* 20:5243–5263.
6. Lanni, F., A. S. Waggoner, and D. L. Taylor. 1985. Structural organization of interphase 3T3 fibroblasts studied by total internal reflection fluorescence microscopy. *J. Cell Biol.* 100:1091–1102.
7. Simon, S. M. 2009. Partial internal reflections on total internal reflection fluorescent microscopy. *Trends Cell Biol.* 19:661–668.
8. Toomre, D., and J. Bewersdorf. 2010. A new wave of cellular imaging. *Annu. Rev. Cell Dev. Biol.* 26:285–314.
9. Schwarz, J. P., I. König, and K. I. Anderson. 2011. Characterizing system performance in total internal reflection fluorescence microscopy. *Methods Mol. Biol.* 769:373–386.
10. Stout, A. L., and D. Axelrod. 1989. Evanescent field excitation of fluorescence by epi-illumination microscopy. *Appl. Opt.* 28:5237–5242.
11. Conibear, P. B., and C. R. Bagshaw. 2000. A comparison of optical geometries for combined flash photolysis and total internal reflection fluorescence microscopy. *J. Microsc.* 200:218–229.
12. Mattheyses, A. L., and D. Axelrod. 2006. Direct measurement of the evanescent field profile produced by objective-based total internal reflection fluorescence. *J. Biomed. Opt.* 11:014006.
13. Mattheyses, A. L., K. Shaw, and D. Axelrod. 2006. Effective elimination of laser interference fringing in fluorescence microscopy by spinning azimuthal incidence angle. *Microsc. Res. Tech.* 69:642–647.
14. van 't Hoff, M., V. de Sars, and M. Oheim. 2008. A programmable light engine for quantitative single molecule TIRF and HILO imaging. *Opt. Express.* 16:18495–18504.
15. Fiolka, R., Y. Belyaev, …, A. Stemmer. 2008. Even illumination in total internal reflection fluorescence microscopy using laser light. *Microsc. Res. Tech.* 71:45–50.
16. Lin, J., and A. D. Hoppe. 2013. Uniform total internal reflection fluorescence illumination enables live cell fluorescence resonance energy transfer microscopy. *Microsc. Microanal.* 19:350–359.
17. Li, D., K. Hérault, …, N. Ropert. 2009. FM dyes enter via a store-operated calcium channel and modify calcium signaling of cultured astrocytes. *Proc. Natl. Acad. Sci. USA.* 106:21960–21965.
18. Dai, L., I. Gregor, …, J. Enderlein. 2005. Measuring large numerical apertures by imaging the angular distribution of radiation of fluorescing molecules. *Opt. Express.* 13:9409–9414.
19. Ridler, T. W., and S. Calvard. 1978. Picture thresholding using an iterative selection method. *IEEE Trans. Syst. Man Cybern.* 8:630–632.
20. Rohrbach, A. 2000. Observing secretory granules with a multiangle evanescent wave microscope. *Biophys. J.* 78:2641–2654.
21. Schapper, F., J. T. Gonçalves, and M. Oheim. 2003. Fluorescence imaging with two-photon evanescent wave excitation. *Eur. Biophys. J.* 32:635–643.
22. Gingell, D., I. Todd, and J. Bailey. 1985. Topography of cell-glass apposition revealed by total internal reflection fluorescence of volume markers. *J. Cell Biol.* 100:1334–1338.
23. Landragin, A., G. Labeyrie, …, A. Aspect. 1996. Specular versus diffuse reflection of atoms from an evanescent-wave mirror. *Opt. Lett.* 21:1591–1593.
24. Chew, H., D.-S. Wang, and M. Kerker. 1979. Elastic scattering of evanescent electromagnetic waves. *Appl. Opt.* 18:2679–2687.
25. Ganic, D., X. Gan, and M. Gu. 2004. Near-field imaging by a microparticle: a model for conversion of evanescent photons into propagating photons. *Opt. Express.* 12:5325–5335.

26. Ambrose, W. P., P. M. Goodwin, and J. P. Nolan. 1999. Single-molecule detection with total internal reflection excitation: comparing signal-to-background and total signals in different geometries. *Cytometry.* 36:224–231.
27. Schneider, R., T. Glaser, …, S. Diez. 2013. Using a quartz paraboloid for versatile wide-field TIR microscopy with sub-nanometer localization accuracy. *Opt. Express.* 21:3523–3539.
28. Blechinger, F., H. Zügge, …, B. Achtner. 2008. Survey of optical instruments. *In* Handbook of Optical Systems, *Vol. 4*. H. Gross, H. Zügge, F. Blechinger, and B. Achtner, editors. Wiley, Weinheim.
29. Oheim, M., and F. Schapper. 2005. Non-linear evanescent-field imaging. *J. Phys. D Appl. Phys.* 38:R185.
30. Lane, R. S. K., A. N. Macpherson, and S. W. Magennis. 2012. Signal enhancement in multiphoton TIRF microscopy by shaping of broadband femtosecond pulses. *Opt. Express.* 20:25948–25959.
31. Chon, J. W. M., M. Gu, …, P. Mulvaney. 2003. Two-photon fluorescence scanning near-field microscopy based on a focused evanescent field under total internal reflection. *Opt. Lett.* 28:1930–1932.
32. Keller, P. J., A. D. Schmidt, …, E. H. Stelzer. 2010. Fast, high-contrast imaging of animal development with scanned light sheet-based structured-illumination microscopy. *Nat. Methods.* 7:637–642.
33. Tokunaga, M., N. Imamoto, and K. Sakata-Sogawa. 2008. Highly inclined thin illumination enables clear single-molecule imaging in cells. *Nat. Methods.* 5:159–161.
34. Hlady, V., D. R. Reinecke, and J. D. Andrade. 1986. Fluorescence of adsorbed protein layers. I. Quantitation of total internal reflection fluorescence. *J. Colloid Interface Sci.* 111:555–569.
35. Ambrose, E. J. 1956. A surface contact microscope for the study of cell movements. *Nature.* 178:1194.
36. Ambrose, E. J. 1961. The movements of fibrocytes. *Exp. Cell Res.* 8 (*Suppl 8*):54–73.
37. Paige, M. F., E. J. Bjerneld, and W. E. Moerner. 2001. A comparison of through-the-objective total internal reflection microscopy and epi-fluorescence microscopy for single-molecule fluorescence imaging. *Single Mol.* 3:191–201.
38. Brunstein M, C. Tourain, M. Oheim. (2012). Glare and other sources of non-evanescent excitation light in objective-type TIRF microscopy. *12th European Light Microscopy Initiative (ELMI) Meeting* (RMS, Leuven). http://arxiv.org/abs/1302.1615.
39. Teremetz, M. 2011. Advantages of spinning TIRF illumination for subcellular fluorescence imaging. Master in Cell Biology and Pathology (BCPP). Université Paris Diderot, Paris.
40. Matsuo, S., and H. Misawa. 2002. Direct measurement of laser power through a high numerical aperture oil immersion objective lens using a solid immersion lens. *Rev. Sci. Instr.* 73:2011–2015.
41. Gingell, D., O. S. Heavens, and J. S. Mellor. 1987. General electromagnetic theory of total internal reflection fluorescence: the quantitative basis for mapping cell-substratum topography. *J. Cell Sci.* 87:677–693.
42. Heavens, O. S. 1995. Use of the approximations in cell studies by total internal reflection fluorescence microscopy (TIRF). *J. Microsc.* 180:106–108.
43. Ölveczky, B. P., N. Periasamy, and A. S. Verkman. 1997. Mapping fluorophore distributions in three dimensions by quantitative multiple angle-total internal reflection fluorescence microscopy. *Biophys. J.* 73:2836–2847.
44. Oheim, M., D. Loerke, …, W. Stühmer. 1998. A simple optical configuration for depth-resolved imaging using variable-angle evanescent-wave microscopy. *Proc. SPIE.* 3568:131–140.
45. Stock, K., R. Sailer, …, H. Schneckenburger. 2003. Variable-angle total internal reflection fluorescence microscopy (VA-TIRFM): realization and application of a compact illumination device. *J. Microsc.* 211:19–29.